
This is an electronic reprint of the original article.
This reprint may differ from the original in pagination and typographic detail.

Mäkinen, J. T.; Autti, S.; Heikkinen, P. J.; Hosio, J. J.; Hänninen, R.; L'vov, V. S.; Walmsley, P. M.; Zavjalov, V. V.; Eltsov, V. B.

Rotating quantum wave turbulence

Published in:
Nature Physics

DOI:
[10.1038/s41567-023-01966-z](https://doi.org/10.1038/s41567-023-01966-z)

Published: 01/06/2023

Document Version
Publisher's PDF, also known as Version of record

Published under the following license:
CC BY

Please cite the original version:
Mäkinen, J. T., Autti, S., Heikkinen, P. J., Hosio, J. J., Hänninen, R., L'vov, V. S., Walmsley, P. M., Zavjalov, V. V., & Eltsov, V. B. (2023). Rotating quantum wave turbulence. *Nature Physics*, 19(6), 898-903.
<https://doi.org/10.1038/s41567-023-01966-z>

This material is protected by copyright and other intellectual property rights, and duplication or sale of all or part of any of the repository collections is not permitted, except that material may be duplicated by you for your research use or educational purposes in electronic or print form. You must obtain permission for any other use. Electronic or print copies may not be offered, whether for sale or otherwise to anyone who is not an authorised user.

Rotating quantum wave turbulence

Received: 9 February 2022

Accepted: 24 January 2023

Published online: 2 March 2023

 Check for updatesJ. T. Mäkinen¹✉, S. Autti^{1,2}, P. J. Heikkinen^{1,3}, J. J. Hosio¹, R. Hänninen^{1,4}, V. S. L'vov⁵, P. M. Walmsley⁶, V. V. Zavjalov^{1,2} & V. B. Eltsov¹

Turbulence under strong influence of rotation is described as an ensemble of interacting inertial waves across a wide range of length scales. In macroscopic quantum condensates, the quasiclassical turbulent dynamics at large scales is altered at small scales, where the quantization of vorticity is essential. The nature of this transition remains an unanswered question. Here we expand the concept of wave-driven turbulence to rotating quantum fluids where the spectrum of waves extends to microscopic scales as Kelvin waves on quantized vortices. We excite inertial waves at the largest scale by periodic modulation of the angular velocity and observe dissipation-independent transfer of energy to smaller scales and the eventual onset of the elusive Kelvin wave cascade at the lowest temperatures. We further find that energy is pumped to the system through a boundary layer distinct from the classical Ekman layer and support our observations with numerical simulations. Our experiments demonstrate a regime of turbulent motion in quantum fluids where the role of vortex reconnections can be neglected, thus stripping the transition between the classical and the quantum regimes of turbulence down to its constituent components.

Rotating turbulence plays an important role in systems such as planets' atmospheres^{1–3}, turbomachinery⁴, rotating quantum gases⁵ and neutron stars^{6,7}. Generally speaking, rotating flows of incompressible classical fluids can be characterized by two dimensionless numbers: the Reynolds number Re denoting the ratio of inertial to dissipative forces, and the Rossby number Ro expressing the ratio of inertial forces to the Coriolis force. In the limit $Re \gg 1$ the flow becomes turbulent, while for $Ro \ll 1$ the rotational effects are important. In superfluids, the Rossby number can be defined in a similar fashion as in classical fluids, while the physical meaning of the Reynolds number is captured by the superfluid Reynolds number Re_α (ref. 8), which only depends on intrinsic mutual friction parameters that describe the coupling between the quantized vortices and the normal component⁹. Theoretical¹⁰, numerical¹¹ and experimental^{12–15} work suggests that, in classical fluids, rotating turbulence, for which $Re \gg 1$ and $Ro \ll 1$, could be described as an ensemble of interacting inertial waves (IWs) plus a broadband turbulent

component, especially for frequencies exceeding twice the angular velocity. The measurements presented here cover $Ro \approx (1–3) \times 10^{-2}$ and $Re_\alpha \approx 10^3–10^5$, which puts our experimental conditions well within the IW turbulence regime.

Quantum turbulence is usually considered as a complex dynamic tangle of reconnecting quantized vortices^{16–19}. In the regime $Re_\alpha \gg 1$ and $Ro \ll 1$, quantized vortices are nearly parallel and inter-vortex reconnections are suppressed²⁰, exposing the underlying wave-turbulent energy cascade to experimental observation. At the largest length scales, the superfluid flow field may mimic that of classical IWs via collective motion of quantized vortices. Contrary to classical fluids, in superfluids the spectrum of waves extends beyond the IW cutoff frequency (Fig. 1a), as Kelvin waves^{21,22} (KWs) carried by individual vortices. The crossover between these regimes takes place at $k_z \ell \approx 0.5$, where k_z is the axial wavevector and ℓ is the mean inter-vortex distance set by the angular velocity.

¹Department of Applied Physics, Aalto University, Aalto, Finland. ²Department of Physics, Lancaster University, Lancaster, UK. ³Department of Physics, Royal Holloway, University of London, Egham, UK. ⁴Finnish Meteorological Institute, Helsinki, Finland. ⁵Department of Chemical Physics, Weizmann Institute of Science, Rehovot, Israel. ⁶Department of Physics and Astronomy, The University of Manchester, Manchester, UK.

✉e-mail: jere.makinen@aalto.fi

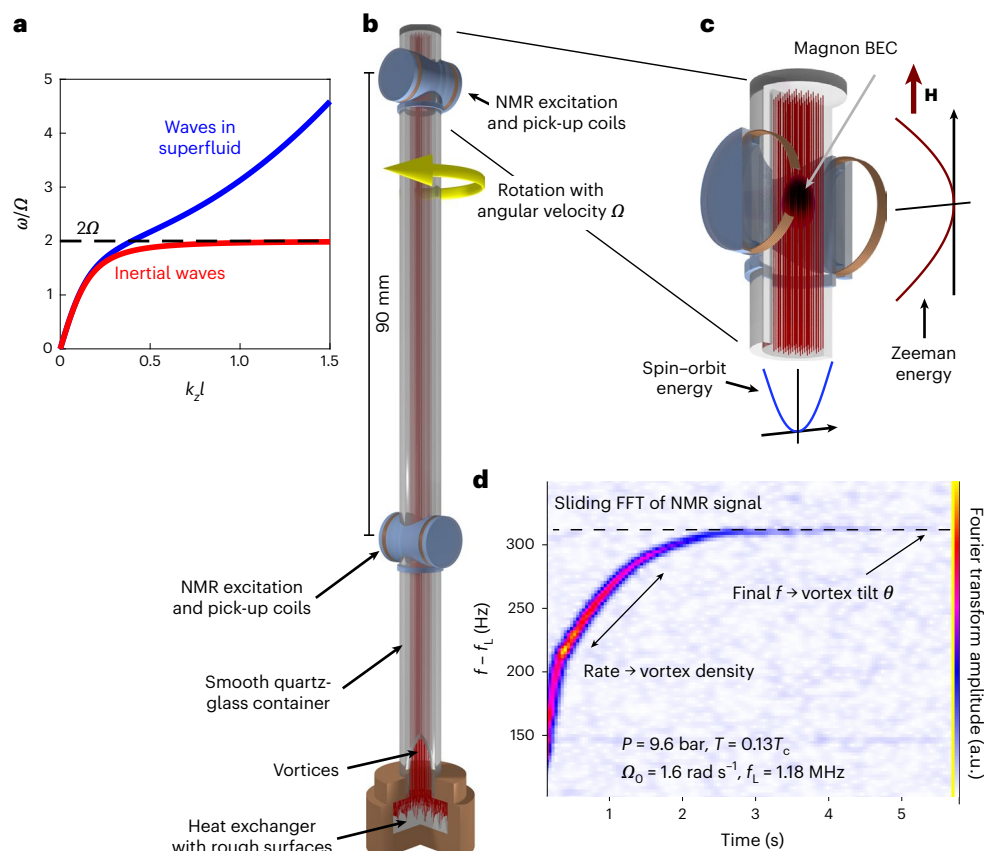


Fig. 1 | Experimental principles. **a**, In superfluids, for fixed radial wavenumber, the full dispersion relation (blue line) extends beyond the classical IW regime (red line) with a cutoff frequency of 2Ω (dashed black line) set by the angular velocity Ω (Supplementary Discussion 3). Here, ω is the angular frequency of the wave mode. **b**, A smooth-walled quartz-glass cylinder, filled with superfluid $^3\text{He-B}$, is rotated about its longitudinal axis. During the experiments, we monitor the vortex configuration at two locations using two pairs of NMR pick-up and excitation coils. The quartz glass container is open from the bottom to a heat exchanger volume with rough silver-sintered surfaces. **c**, The spatial distribution

of vortices is monitored with a magnon BEC, trapped in the axial direction in a minimum of the magnetic field \mathbf{H} and in the radial direction by spatial variation of the spin-orbit energy (called texture). The radial trapping potential is modified by the presence of vortices. **d**, We use pulsed NMR to probe the ground-state frequency in the magneto-textural trap. The frequency is shown as the shift from the Larmor frequency f_L . The relaxation rate of the signal depends on the vortex density³⁴, while the final frequency (dashed line) is affected by the orientation of vortices (Supplementary Discussion 1).

To highlight differences between classical and quantum turbulence, the low-temperature limit is of particular interest since negligible frictional forces allow transfer of energy to length scales where quantization of vorticity is essential^{19,23}. In this limit, the energy is believed to flow towards the smallest scales through a cascade of KWs^{24,25} or through a quantum stress cascade²⁶ and is ultimately dissipated via emission of sound waves²⁷, emission of quasiparticles^{28,29} or, at a finite temperature, mutual friction^{9,30}. Despite observations of vortex reconnections and the related production of KWs^{31,32}, direct experimental proof of the existence of the KW cascade has remained elusive.

In the experiments, we initially rotate the sample volume (Fig. 1b) with a constant angular velocity to create an array of quantized vortices with aerial density ℓ^{-2} oriented along the axis of rotation. We monitor the vortex configuration independently at two spatially separated locations (Fig. 1c) via pulsed NMR techniques (Fig. 1d). We then perturb the vortex array by applying a time-dependent angular drive $\Omega(t) = \Omega_0 + \Omega_1 f(\omega_{\text{ex}} t)$, where Ω_0 is the mean angular velocity during the drive with amplitude $\Omega_1 < \Omega_0$, and f denotes a triangle wave in the range $[-1, 1]$ with period $p = 2\pi\omega_{\text{ex}}^{-1}$. During the drive, the following forces are exerted on the vortices: the force due to mutual friction, the Magnus force and the force due to pinning of the vortex ends at the rough bottom of the container. Elsewhere, the smooth walls of the cylinder allow nearly frictionless vortex sliding³³. We note that, while

the upper spectrometer is located much closer to a surface than the bottom one, the response to the drive (Fig. 2a) is observed first in the bottom spectrometer. This suggests that the coupling between the quantized vortices and the (smooth) top surface is negligible in comparison with that between the vortices and the (rough) bottom surface. Even smoother surfaces may be produced in cold atom experiments, where a uniform trapping potential can be provided by repulsive laser light.

Soon after we start the time-dependent drive, we observe a decrease in the measured NMR frequency (Fig. 2a) resulting from an increased average vortex tilt angle with respect to the axis of rotation, denoted by θ (Supplementary Discussion 1). Notably, a propagating wavefront originates from the bottom of the container with phase velocity $V_{\text{prop}} \approx 0.3 \text{ cm s}^{-1}$. This velocity agrees with the phase velocity of the first axially symmetric radial inertial wave mode, $V_{\text{ph}} = \omega_{\text{ex}}/k_z \approx 0.25 \text{ cm s}^{-1}$. Simultaneously, we observe no change in the relaxation rate of the NMR signal, indicating that the vortex density remains constant during this time³⁴. These observations are in sharp contrast to spin-down measurements with the same experimental setup^{9,35}, where the container is abruptly brought to rest. In response to the spin down, the total angular velocity of the superfluid relaxes towards zero and the initial equilibrium vortex configuration quickly turns to 3D quantum turbulence governed by vortex reconnections and characterized by $t^{-3/2}$ decay of the vortex line length.

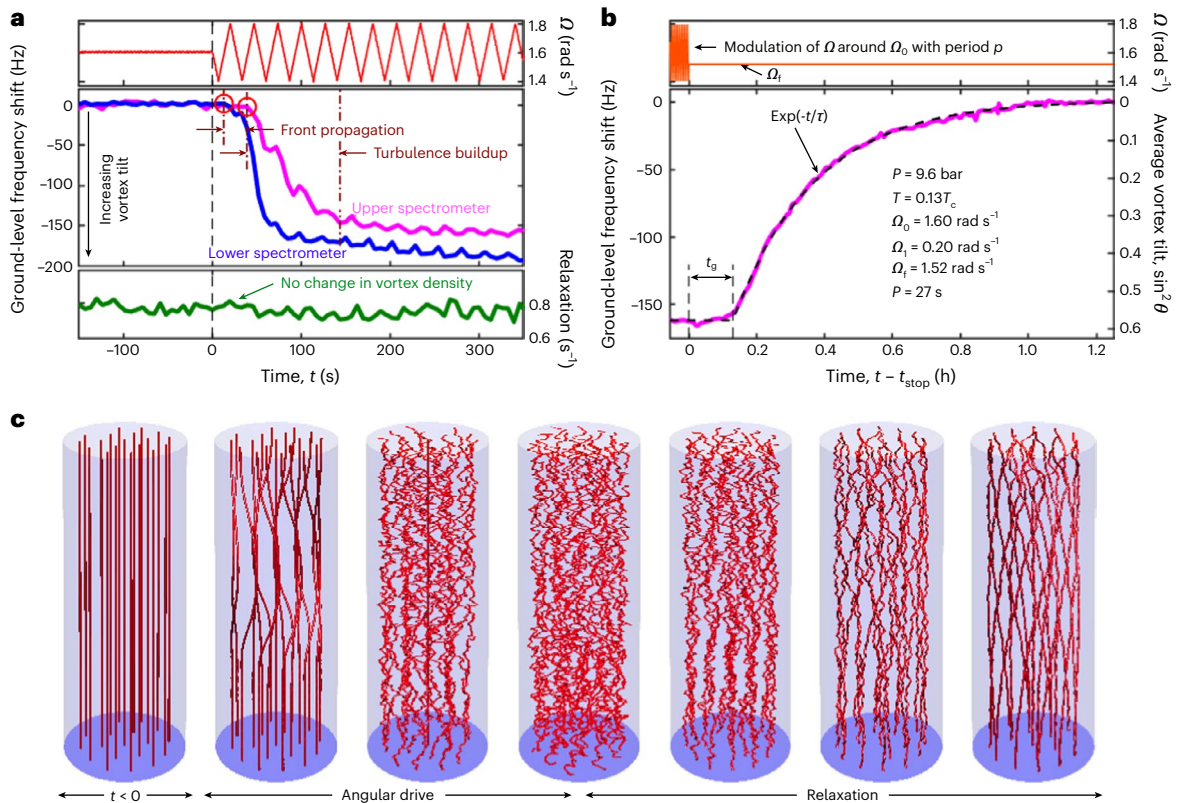


Fig. 2 | Buildup and decay of rotating quantum wave turbulence. **a**, Modulation of the angular velocity (top panel) results in a propagating front of increasing vortex tilt, seen as a frequency shift in NMR measurements (middle panel). The front velocity and saturation time of the signal are explained by the dynamics of IWs (Supplementary Discussion 4). The NMR relaxation rate in the lower spectrometer (bottom panel) shows no observable change in the response to the drive, indicating that the vortex density remains constant during this time³⁴. **b**, At time t_{stop} , the drive is ramped to a final angular velocity Ω_f using the same acceleration $\dot{\Omega}$ as during the modulations. After that, an initial period of duration t_g , during which the average vortex tilt angle θ remains at a level comparable to the developed turbulence, is followed by an exponential decay towards the

equilibrium state. Our estimate (Supplementary Discussions 1 and 7) for the mean vortex tilt angle within the upper spectrometer in units of $\sin^2\theta$ is shown on the right axis. **a** and **b** correspond to the same experimental run with $t_{\text{stop}} \approx 1.0$ h. **c**, We utilize vortex filament simulations to visualize our experiment. In the simulations, vortex lines (red) in a cylindrical container (light blue, $L = 50$ mm) are driven out of equilibrium by applying a drive similar to that in the experiments. In simulations, the vortices couple to the drive via a thin layer with high mutual friction at the bottom (dark blue). The figures are not drawn to scale. The mean inter-vortex distance is $\ell \approx 0.1$ mm. The horizontal alignment of the figures corresponds to the state of the experiment immediately above.

During the drive, the action of hydrodynamic forces on a vortex would far exceed the maximum pinning force, equal to the vortex tension $T_v \approx 10^{-8}$ cm g s⁻². In this case, vortices are inevitably stretched and the rotating superfluid forms a quantum boundary layer, previously discussed in ref. 36, in which each vortex is acted upon with force equal in magnitude to T_v . We describe the flow of energy in such a system using a phenomenological model (Supplementary Discussion 2) in which the quantum boundary layer pumps energy to a cascade of IWs³⁷, which in turn feeds a cascade of KWs. In the KW regime, the energy is consumed by mutual friction, which also terminates the KW cascade. A qualitatively similar picture is obtained in vortex filament calculations in the presence of a surface layer with increased mutual friction (Fig. 2c). The calculations demonstrate how, in response to the drive, vortices, initially excited at the long wavelength limit, transfer energy towards smaller scales while the role of vortex reconnections is negligible. This process resembles earlier numerical simulations of the cascade of Kelvin waves generated from the excitation of a single KW mode,³⁸ but applied here for a vortex bundle which supports IWs in the long wavelength limit.

After the system has reached a steady state, we stop the drive and ramp the angular velocity to a chosen value Ω_f that may differ from Ω_0 . The vortex array then relaxes from its steady-state configuration with $\theta \approx 50^\circ$ towards the equilibrium state with $\theta \rightarrow 0$ via a

process comprising two clearly distinct stages (Fig. 2b). In the first stage, θ remains at a similar level as during the drive. During this interval, marked as t_g , large vortex tilt is sustained by feeding the global flow energy via the quantum boundary layer to IWs (and subsequently to KWs via the IW cascade). The second relaxation stage, an exponential restoration of the equilibrium vortex configuration of the form $\sin^2\theta \propto \exp(-t/\tau)$ with time constant τ , expected for decaying KWs, is observed after the energy from the global flow has been consumed. This exponential decay is related to dissipation of the energy stored in the KW cascade by mutual friction and qualitatively reproduced in our model calculations (Supplementary Discussion 8 and Supplementary Fig. 8).

The duration of the first relaxation stage is set by the amount of energy stored in the solid-body-like flow and controlled experimentally by varying the final angular velocity Ω_f . The characteristic time $t_g(\Omega_f)$ increases with increasing $|\Omega_f - \Omega_0|$ (Fig. 3a). If each vortex is acted upon in a boundary layer with a force equal to βT_v in magnitude, the superfluid angular velocity reaches Ω_f in a finite time $t_g^* = \beta^{-1}\tau_s |\ln(\Omega_f/\Omega_0)|$, where $\tau_s \approx 4 \times 10^3$ s (Supplementary Discussion 2) and the fitting parameter $\beta \approx 1$ characterizes the energy pumping efficiency. The expression for t_g^* agrees with our observations of t_g with a single fitted β in the temperature range of (0.13–0.19) T_c , where $T_c \approx 1$ mK is the superfluid transition temperature of ³He. Over this temperature range, the

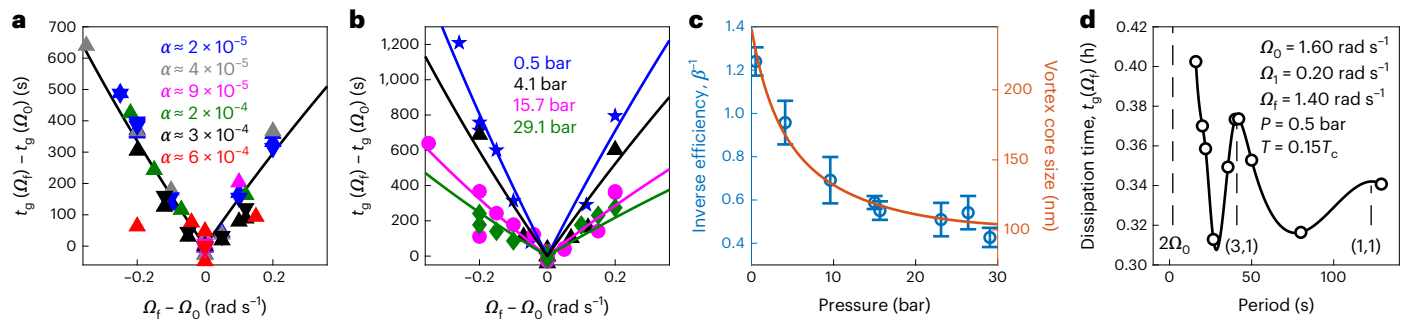


Fig. 3 | Transfer of energy through the quantum boundary layer. **a**, The observed relaxation times of the energy stored in solid-body-like rotating flow (symbols) compared with the model of pumping by the quantum boundary layer characterized by the time τ_g^* (solid black line). Here, $\Omega_0 = 1.6 \text{ rad s}^{-1}$, $\Omega_1 = 0.20 \text{ rad s}^{-1}$, $p = 27 \text{ s}$ and the fitted energy pumping efficiency is $\beta^{-1} = 0.57$. The data include measurements at pressures of 15.0 and 15.7 bar. We plot the difference $t_g(\Omega_f) - t_g(\Omega_0)$, where $t_g(\Omega_0)$ is separately measured with $\Omega_f = \Omega_0$, to account for any excess energy (such as near-resonant inertial waves or geostrophic modes) not present in our model. Different colours correspond to different temperatures in the range $(0.14\text{--}0.19)T_c$ and thus values of the mutual friction parameter α , as marked in the figure. Upwards-pointing triangles

correspond to data measured with the upper spectrometer, while downwards-pointing triangles correspond to data from the lower spectrometer. **b**, The pumping efficiency is found to change with pressure. **c**, The observed increase of β with pressure (symbols, left axis) may be understood via enhanced pinning with decreasing vortex core size³⁹ (solid line, right axis). **d**, Measurements of t_g with different period of excitation show an increase in the stored energy in the presence of standing inertial waves. The IW cutoff frequency and the modes (M, N) , where M is the axial and N is the radial wavenumber, are marked with vertical dashed lines. The error bars in **c** correspond to 1σ confidence intervals. The estimated error in determining t_g is smaller than the symbol size, and errors in **a**, **b** and **d** are not drawn.

dissipative mutual friction parameter α , which controls the energy dissipation rate in the bulk, changes by almost two orders of magnitude⁹. This temperature independence confirms our picture of the quantum boundary layer feeding the IW energy cascade. As a function of pressure P , the observed change in β (Figs. 3b,c) could be explained by the change in the vortex core size³⁹ with the premise that smaller core size results in enhanced pinning. Furthermore, the complicated dependence of t_g on ω_{ex} (Fig. 3d) may be understood as additional contributions to the energy of the global flow in the vicinity of standing axially symmetric inertial wave resonances in the cylindrical sample container^{40,41} and possible generation of geostrophic modes^{14,15}.

Let us now turn our attention to the second relaxation stage. For a single KW with a wavevector k , the energy dissipation rate by mutual friction is exponential with a decay rate⁴² $\tau_{\text{mf}}^{-1} = 2\alpha v_s k^2$, where $v_s \approx 4 \times 10^{-4} \text{ cm}^2 \text{ s}^{-1}$. On the other hand, for a distribution of KWs in the form of a cascade extending between k_{start} and $k_{\text{end}} \gg k_{\text{start}}$, the dissipation remains exponential with a rate given by $\tau_{\text{LN}}^{-1} = \alpha v_s k_{\text{start}}^{2/3} k_{\text{end}}^{1/3}$ (assuming a L'vov–Nazarenko KW spectrum;²⁵ Supplementary Discussions 5 and 6). To distinguish between the single-scale and distribution-of-scales scenarios, we study the dependence of the experimental time constant τ^{-1} on the rotation velocity and temperature. We find that the relaxation rate is linearly proportional to Ω_f at a constant temperature (constant α). That is, that $\tau^{-1} \equiv \mathcal{A}\Omega_f$, where \mathcal{A} is a constant (Fig. 4a), suggesting that the dissipative length scale is set by $\ell^{-1} \propto \sqrt{\Omega_f}$. Therefore, in the absence of a cascade for a fixed $k\ell$ (fixed k^2/Ω_f), \mathcal{A} is expected to scale linearly with α . We find that, at higher values of α (higher temperatures), \mathcal{A} is roughly linear in α (Fig. 4b). In this range, we assume that the dissipation is asymptotically given by a single length scale, that is, $k_{\text{start}} = k_{\text{end}}$. Using values of α from ref. 9 (with $\alpha = 0$ at $T = 0$) and the measured values of \mathcal{A} , we find $k_{\text{start}} = 2.3\ell^{-1}$. However, the deviation from the linear dependence towards the lowest α (lowest temperatures) implies that the dissipation length scale changes with temperature. In the KW cascade picture, this is naturally explained by extension of the cascade towards larger k_{end} with decreasing α (ref. 30). Setting $\tau^{-1} = \tau_{\text{LN}}^{-1}$ and using the estimated value for k_{start} , we obtain the extent of the KW cascade $k_{\text{end}}/k_{\text{start}}$ (Fig. 4c). The cascade quickly expands to larger wavevectors for $\alpha \lesssim 10^{-4}$, in agreement with previous numerical simulations⁴³.

Our experimental observations, namely that $\tau \propto \Omega_f^{-1} \propto \ell^{-2}$ and that τ tends towards a constant value at the lowest α , are consistent with

theoretical predictions²⁰ linking the extent of the KW cascade to the effective kinematic viscosity ν' used to characterize the energy dissipation rate in quantum turbulence (Supplementary Discussion 5). Using the lowest temperature data in Fig. 4b, we obtain an estimate $\nu' \approx 10^{-6} \kappa$, where $\kappa \approx 6.6 \times 10^{-4} \text{ cm}^2 \text{ s}^{-1}$ is the quantum of circulation in ^3He . The obtained value is five orders of magnitude smaller than for homogeneous and isotropic quantum turbulence⁴⁴, highlighting the different nature of the turbulent flows. Smaller values of ν' are generally thought to originate from nearly parallel arrangement of vortices²⁰ and in the absence of vortex reconnections⁴⁵, both of which are realized in our experiments. We also note that, while a recent theoretical work²⁶ put forward an idea of a ‘quantum stress cascade’ as a possible energy transfer mechanism, our observations—in particular the magnitude of the average vortex tilt θ determined mostly by KWs, the temperature dependence of the dissipative length scale, and the wavevector range of the excited KWs from k_{start} to k_{end} —imply the picture involving a cascade of KWs. We note that, while we cannot experimentally distinguish between different proposed theoretical models for the KW cascade^{24,25,38}, the qualitative result (extension of the KW cascade further in k -space for lower α) is valid regardless of the model (Supplementary Discussion 6 and Supplementary Fig. 7). In the future, detailed numerical simulations of the suppression of the KW cascade by mutual friction in a setting similar to that in our experiment might allow discrimination between models based on our experimental input. Finally, we note that the outliers in the higher temperature data in Figs. 3 and 4 may indicate that the KW cascade picture changes with increasing temperature for $\alpha \gtrsim 10^{-3}$ where the dissipative length scale, set by mutual friction, crosses over from quantum ($\lesssim \ell$) to classical ($\gtrsim \ell$) length scales and the KW cascade is completely suppressed.

In a historical context, our work relates to the centuries-old d’Alembert’s paradox stating that, for incompressible potential flow (applicable also to a superfluid), there is no drag for a body moving with constant velocity within the fluid. The solution to this apparent paradox was introduced by Prandtl, who noted that the coupling between the moving body and the surrounding fluid originates in thin surface layers. For rotating flows in classical systems such as the atmosphere or oceans, as a result of a ‘no-slip’ boundary condition, the surface layer takes the form of an Ekman layer. Our experimental findings in the presence of a rough surface are consistent with a ‘partial-slip’ quantum boundary layer, unique to superfluids, where the magnitude of the

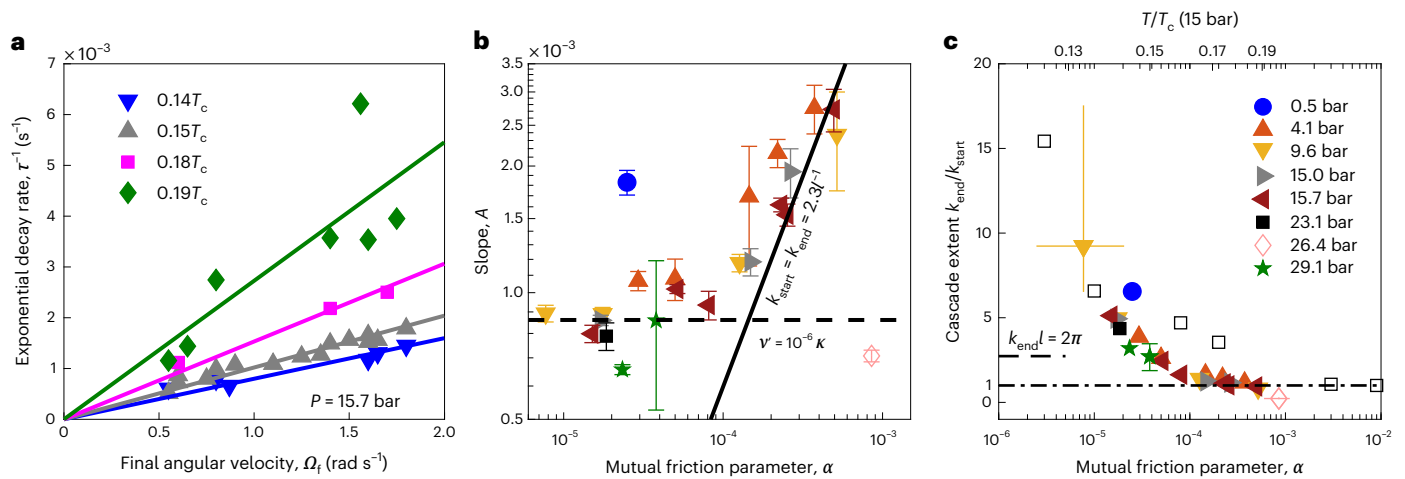


Fig. 4 | Formation of the KW cascade with decreasing temperature. **a**, The observed exponential relaxation time scales as $\tau^{-1} = \mathcal{A}\Omega_f$. In contrast to the temperature-independent t_g (Fig. 3a), the relaxation becomes faster at higher temperatures. $\Omega_1 = 0.2 \text{ rad s}^{-1}$ and $\Omega_0\Omega_1^{-1} \approx 53$ were kept constant. The error in τ^{-1} is smaller than the symbol size, and error bars are not shown. **b**, The mutual-friction dependence of the relaxation rate normalized to Ω_f , that is, the slopes \mathcal{A} in **a**, deviate from the linear dependence expected for a fixed dissipative length scale (solid line), suggesting that the effective dissipative length scale is changing with temperature as a result of the KW cascade. From data at the lowest temperatures, we estimate the value of the effective kinematic viscosity ν' (dashed line) (Supplementary Discussion 5). The error bars correspond to 1σ confidence intervals. **c**, We extract the KW cascade extent (filled symbols and

open diamond) in the k space as discussed in the main text. The dot-dashed line corresponds to the single-scale scenario with $k_{end} = k_{start}$ (same as solid line in **b**). The cascade extends further in the k space with decreasing α , in line with numerical simulations from ref. 43 (open squares). At the lowest temperatures ($\alpha \lesssim 3 \times 10^{-5}$), the KW cascade extends to the length scales smaller than the inter-vortex distance (short dashed line). The largest statistical error from **b** is shown for the corresponding point (29.1 bar). For other points, the statistical errors are smaller than the symbol size. The highest temperature (26.4 bar) and lowest temperature (9.6 bar) points display the estimated systematic errors (Methods) in α , drawn as capless error bars. Symbol colours in **b** and **c** mark different pressures shown in the key in **c**.

applied force per quantized vortex is limited to a constant value. On the other hand, superfluids in the zero temperature limit may allow for experimental realization of the original d'Alembert's paradox in the presence of a smooth surface or if vortices are immobilized in the whole volume, for example, by a nano-structured confinement⁴⁶. In this work, the presence of the quantum boundary layer allows us to excite vortex waves, which develop into a novel type of quantum turbulence driven by non-linear interactions between vortex waves instead of vortex reconnections. Finally, the measurements presented in Fig. 4b support the existence of the dissipative anomaly for a cascade of KWs. The dissipative anomaly is also referred to as the zeroth law of turbulence due to its fundamental importance for the turbulence theory, and it states that dissipation should remain finite even in the limit of vanishing viscosity (or infinite Reynolds number). However, its nature and very existence for various forms of turbulence is still an active topic of research^{47,48}.

Online content

Any methods, additional references, Nature Portfolio reporting summaries, source data, extended data, supplementary information, acknowledgements, peer review information; details of author contributions and competing interests; and statements of data and code availability are available at <https://doi.org/10.1038/s41567-023-01966-z>.

References

- Hoekstra, A., Derksen, J. & Van Den Akker, H. An experimental and numerical study of turbulent swirling flow in gas cyclones. *Chem. Eng. Sci.* **54**, 2055–2065 (1999).
- Sommeria, J., Meyers, S. D. & Swinney, H. L. Laboratory simulation of Jupiter's Great Red Spot. *Nature* **331**, 689–693 (1988).
- Marcus, P. S. Numerical simulation of Jupiter's Great Red Spot. *Nature* **331**, 693–696 (1988).
- Bradshaw, P. Turbulence modeling with application to turbomachinery. *Prog. Aerosp. Sci.* **32**, 575–624 (1996).
- Hossain, K. et al. Rotating quantum turbulence in unitary Fermi gas. *Phys. Rev. A* **105**, 013304 (2022).
- Greenstein, G. Superfluid turbulence in neutron stars. *Nature* **227**, 791–794 (1970).
- Andersson, N., Sidery, T. & Comer, G. L. Superfluid neutron star turbulence. *Mon. Not. R. Astron. Soc.* **381**, 747–756 (2007).
- Finne, A. P. et al. Dynamics of vortices and interfaces in superfluid ³He. *Rep. Prog. Phys.* **69**, 3157 (2006).
- Mäkinen, J. T. & Eltsov, V. B. Mutual friction in superfluid ³He-B in the low-temperature regime. *Phys. Rev. B* **97**, 014527 (2018).
- Galtier, S. Weak inertial-wave turbulence theory. *Phys. Rev. E* **68**, 015301 (2003).
- Bellet, F., Godeferd, F. S., Scott, J. F. & Cambon, C. Wave turbulence in rapidly rotating flows. *J. Fluid Mech.* **562**, 83–121 (2006).
- Yarom, E. & Sharon, E. Experimental observation of steady inertial wave turbulence in deep rotating flows. *Nat. Phys.* **10**, 510–514 (2014).
- Yarom, E., Salhov, A. & Sharon, E. Experimental quantification of nonlinear time scales in inertial wave rotating turbulence. *Phys. Rev. Fluids* **2**, 122601 (2017).
- Monsalve, E., Brunet, M., Gallet, B. & Cortet, P.-P. Quantitative experimental observation of weak inertial-wave turbulence. *Phys. Rev. Lett.* **125**, 254502 (2020).
- Brunet, M., Gallet, B. & Cortet, P.-P. Shortcut to geostrophy in wave-driven rotating turbulence: the quartet instability. *Phys. Rev. Lett.* **124**, 124501 (2020).
- Walmsley, P. M. & Golov, A. I. Coexistence of quantum and classical flows in quantum turbulence in the $T=0$ limit. *Phys. Rev. Lett.* **118**, 134501 (2017).
- Walmsley, P. M. & Golov, A. I. Quantum and quasiclassical types of superfluid turbulence. *Phys. Rev. Lett.* **100**, 245301 (2008).

18. Cidrim, A., White, A. C., Allen, A. J., Bagnato, V. S. & Barenghi, C. F. Vinen turbulence via the decay of multicharged vortices in trapped atomic Bose–Einstein condensates. *Phys. Rev. A* **96**, 023617 (2017).
19. Barenghi, C. F., Skrbek, L. & Sreenivasan, K. R. Introduction to quantum turbulence. *Proc. Natl Acad. Sci. USA* **111**, 4647–4652 (2014).
20. L'vov, V. S., Nazarenko, S. V. & Rudenko, O. Bottleneck crossover between classical and quantum superfluid turbulence. *Phys. Rev. B* **76**, 024520 (2007).
21. Thomson, S. W. XXIV. Vibrations of a columnar vortex. *Lond. Edinb. Dublin Philos. Mag. J. Sci.* **10**, 155–168 (1880).
22. Henderson, K. L. & Barenghi, C. F. Vortex waves in a rotating superfluid. *Europhys. Lett.* **67**, 56 (2004).
23. Skrbek, L., Schmoranzler, D., Midlik, Š. & Sreenivasan, K. R. Phenomenology of quantum turbulence in superfluid helium. *Proc. Natl Acad. Sci. USA* **118**, e2018406118 (2021).
24. Kozik, E. & Svistunov, B. Kelvin-wave cascade and decay of superfluid turbulence. *Phys. Rev. Lett.* **92**, 035301 (2004).
25. L'vov, V. S. & Nazarenko, S. Spectrum of Kelvin-wave turbulence in superfluids. *JETP Lett.* **91**, 428–434 (2010).
26. Tanogami, T. Theoretical analysis of quantum turbulence using the Onsager ideal turbulence theory. *Phys. Rev. E* **103**, 023106 (2021).
27. Vinen, W. F. How is turbulent energy dissipated in a superfluid? *J. Phys. Condens. Matter* **17**, S3231–S3238 (2005).
28. Silaev, M. A. Universal mechanism of dissipation in fermi superfluids at ultralow temperatures. *Phys. Rev. Lett.* **108**, 045303 (2012).
29. Kopnin, N. B. & Salomaa, M. M. Mutual friction in superfluid ^3He : effects of bound states in the vortex core. *Phys. Rev. B* **44**, 9667–9677 (1991).
30. Boué, L., L'vov, V. & Procaccia, I. Temperature suppression of Kelvin-wave turbulence in superfluids. *Europhys. Lett.* **99**, 46003 (2012).
31. Bewley, G. P., Paoletti, M. S., Sreenivasan, K. R. & Lathrop, D. P. Characterization of reconnecting vortices in superfluid helium. *Proc. Natl Acad. Sci. USA* **105**, 13707–13710 (2008).
32. Fonda, E., Meichle, D. P., Ouellette, N. T., Hormoz, S. & Lathrop, D. P. Direct observation of Kelvin waves excited by quantized vortex reconnection. *Proc. Natl Acad. Sci. USA* **111**, 4707–4710 (2014).
33. Hosio, J. J. et al. Energy and angular momentum balance in wall-bounded quantum turbulence at very low temperatures. *Nat. Commun.* **4**, 1614 (2012).
34. Autti, S. et al. Vortex-mediated relaxation of magnon BEC into light Higgs quasiparticles. *Phys. Rev. Res.* **3**, L032002 (2021).
35. Hosio, J. J., Eltsov, V. B., Krusius, M. & Mäkinen, J. T. Quasiparticle-scattering measurements of laminar and turbulent vortex flow in the spin-down of superfluid $^3\text{He-B}$. *Phys. Rev. B* **85**, 224526 (2012).
36. Adams, P. W., Cieplak, M. & Glaberson, W. I. Spin-up problem in superfluid ^4He . *Phys. Rev. B* **32**, 171–177 (1985).
37. Alexakis, A. & Biferale, L. Cascades and transitions in turbulent flows. *Phys. Rep.* **767–769**, 1–101 (2018).
38. Vinen, W. F., Tsubota, M. & Mitani, A. Kelvin-wave cascade on a vortex in superfluid ^4He at a very low temperature. *Phys. Rev. Lett.* **91**, 135301 (2003).
39. Silaev, M. A., Thuneberg, E. V. & Fogelström, M. Lifshitz transition in the double-core vortex in $^3\text{He-B}$. *Phys. Rev. Lett.* **115**, 235301 (2015).
40. Fultz, D. A note on overstability and the elastoid-inertia oscillations of Kelvin, Solberg, and Bjerknes. *J. Meteorol.* **16**, 199–208 (1959).
41. Walmsley, P. M. & Golov, A. I. Rotating quantum turbulence in superfluid ^4He in the $T=0$ limit. *Phys. Rev. B* **86**, 060518 (2012).
42. Donnelly, R. J. *Quantized Vortices in Helium II* (Cambridge Univ. Press, 1991).
43. Boué, L. et al. Energy and vorticity spectra in turbulent superfluid ^4He from $T=0$ to T_λ . *Phys. Rev. B* **91**, 144501 (2015).
44. Gao, J., Guo, W. & Vinen, W. F. Determination of the effective kinematic viscosity for the decay of quasiclassical turbulence in superfluid ^4He . *Phys. Rev. B* **94**, 094502 (2016).
45. Leadbeater, M., Samuels, D. C., Barenghi, C. F. & Adams, C. S. Decay of superfluid turbulence via Kelvin-wave radiation. *Phys. Rev. A* **67**, 015601 (2003).
46. Autti, S. et al. Exceeding the Landau speed limit with topological Bogoliubov Fermi surfaces. *Phys. Rev. Res.* **2**, 033013 (2020).
47. Panickacheril John, J., Donzis, D. A. & Sreenivasan, K. R. Does dissipative anomaly hold for compressible turbulence? *J. Fluid Mech.* **920**, A20 (2021).
48. Galantucci, L., Rickinson, E., Baggaley, A. W., Parker, N. G. & Barenghi, C. F. Dissipation anomaly in a turbulent quantum fluid. Preprint at *arXiv* <https://arxiv.org/abs/2206.14030> (2022).

Publisher's note Springer Nature remains neutral with regard to jurisdictional claims in published maps and institutional affiliations.

Open Access This article is licensed under a Creative Commons Attribution 4.0 International License, which permits use, sharing, adaptation, distribution and reproduction in any medium or format, as long as you give appropriate credit to the original author(s) and the source, provide a link to the Creative Commons license, and indicate if changes were made. The images or other third party material in this article are included in the article's Creative Commons license, unless indicated otherwise in a credit line to the material. If material is not included in the article's Creative Commons license and your intended use is not permitted by statutory regulation or exceeds the permitted use, you will need to obtain permission directly from the copyright holder. To view a copy of this license, visit <http://creativecommons.org/licenses/by/4.0/>.

© The Author(s) 2023, corrected publication 2023

Methods

Sample geometry and thermometry

Our choice of liquid is the superfluid B phase of ^3He , which can be studied by using non-invasive NMR methods and for which the low-temperature limit is experimentally accessible. The sample is confined within a 150-mm-long cylindrical container with $\varnothing 5.85$ mm inner diameter, made from quartz glass (Fig. 1b,c). To avoid vortex pinning on the walls of the container, its inner surfaces are treated with hydrofluoric acid⁴⁹. The experimental volume, filled with ^3He -B, is open from the bottom for thermal coupling to the nuclear demagnetization stage. The experimental volume contains two commercial quartz tuning forks with 32 kHz resonance frequency, commonly used for thermometry in ^3He experiments^{50,51}. The forks are calibrated against the Leggett frequency of ^3He -B, found by continuous-wave NMR spectroscopy at $0.37T_c$ and 0.5 bar. At lower temperatures, we assume that the forks' behaviour is limited to the ballistic regime of quasiparticle propagation, where the forks' resonance width behaves as c , where k_B is the Boltzmann constant. The parameter $c \approx 10 \pm 1.5$ kHz is the geometric factor, and $\Delta f_0 \approx 10$ – 100 mHz, determined by comparison with magnetic relaxation of the magnon Bose–Einstein condensate (BEC)⁵², is the forks' intrinsic width. The calibration is extrapolated to other pressures assuming $c \propto p_F^4$ (ref. 53), where p_F is the Fermi momentum.

NMR spectroscopy

Vortex lines affect the spatial order parameter distribution (texture) in superfluid ^3He -B owing to contributions from the vortex cores and superflow around them⁵⁴. Information about the order parameter texture can be extracted via magnetic quasiparticles, magnons, pumped to a three-dimensional trapping potential with a radiofrequency pulse. The magnons quickly form a uniformly precessing BEC in the trap formed by the order parameter texture in the radial direction and by a minimum of the magnetic field in the axial direction. The amplitude of the NMR signal depends on the number of magnons in the trap, which also affects the frequency of the signal. In rotation and at low temperatures, the lifetime of magnons in the trap is limited by conversion to other spin-wave modes mediated by vortices. Thus, the decay time of the NMR signal is a measure of the vortex line density⁵⁵. Simultaneously, vortex orientation affects the textural part of the magnon trap and the energy of the ground state in the trap, which modifies the precession frequency of the magnon BEC seen in NMR.

In the measurements, we use a static magnetic field of 25 and 36 mT in the upper and lower spectrometer, respectively. The corresponding NMR frequencies are 830 kHz and 1.2 MHz. The magnetic field is created using coils whose symmetry axis is aligned along the axis of rotation. The NMR pick-up coils are spatially separated along the axis of rotation by 90 mm, oriented perpendicular to one another and perpendicular to the axis of rotation. The upper pick-up coil is made of copper wire and is a part of the tank circuit with a quality factor of $Q \approx 1.5 \times 10^2$. The lower pick-up coil is made of superconducting wire and is a part of the tank circuit with a quality factor of $Q \approx 7.5 \times 10^3$. We use cold pre-amplifiers, thermalized to a bath of liquid helium, and room-temperature pre-amplifiers, to improve the signal-to-noise ratio in the measurements.

Rotating refrigerator

The sample can be rotated about its vertical axis with angular velocities up to 3 rad s^{-1} , and cooled down to approximately $150 \mu\text{K}$ by using a ROTA nuclear demagnetization refrigerator. The refrigerator is well balanced and suspended against vibrational noise. The Earth's magnetic field is compensated using two saddle-shaped coils installed around the refrigerator to avoid parasitic heating of the nuclear stage. In rotation, the total heat leak to the sample remains below 20 pW (ref. 56). The rotation velocity is typically changed with a rate of $|\dot{\Omega}| = 0.03 \text{ rad s}^{-2}$.

Vortex filament simulations

Vortex filament simulations^{57,58}, based on the Biot–Savart law, are used to support our qualitative interpretation of the experimental observations. The simulations start with 19 vortices distributed in three rings with 1, 6 and 12 vortices, from innermost to outermost ring, respectively. Initially, the vortices are straight and terminate at the top and bottom walls, spanning a total of 50 mm each with spatial resolution of 0.125 mm. We note that this resolution is insufficient to reliably determine the spectrum of KWs from simulations. The initial separation of the straight vortices corresponds to a rotating drive of 1.60 rad s^{-1} . The sample radius is 1 mm, and to reduce the computational complexity, vortices occupy only a fraction of the cross-section of the cylinder. An external periodic drive between 1.40 and 1.80 rad s^{-1} with acceleration of 0.03 rad s^{-2} is used to drive the vortices out of equilibrium. Image vortices are used to prevent flow through the boundaries.

The vortices couple to the external drive via mutual friction. The mutual friction parameter takes the value $\alpha = 1.77 \times 10^{-3}$ in the bulk. Additionally, we set $\alpha = 2$ within a 0.1 mm layer at the bottom (Fig. 2c, dark blue). At $\alpha \gg 1$, vortices move with the normal component, which in this simulation is clamped to the container. We found that $\alpha = 2$ is sufficient to keep vortex ends fixed with respect to the bottom boundary, which emulates pinning as seen in the experiment. In simulations, we observe an upwards-propagating wave similar to the experiments and the eventual development of vortex waves at small scales. We further note that producing a layer with high mutual friction experimentally is possible by applying a suitable magnetic field to create a layer of the superfluid A phase with high mutual friction.

During the drive in the simulations (which was on for 600 s), there are a total of 127 inter-vortex reconnection events (using $40 \mu\text{m}$ as the reconnection distance), with an average reconnection rate of approximately $2 \times 10^{-3} \text{ cm}^{-1} \text{ s}^{-1}$. Averaging over 20 s intervals, the highest reconnection rate per vortex length is approximately $10^{-2} \text{ cm}^{-1} \text{ s}^{-1}$ or about one reconnection every 20 s per vortex. In addition, small-scale structures appear before the first reconnection event takes place, suggesting that inter-vortex reconnections do not play a significant role in the development of the cascade. When the modulation of the rotation velocity is stopped (here, $\Omega_f = \Omega_0$), the vortex configuration decays towards the equilibrium state with parallel straight vortices. To reduce the computation time for illustrative purposes, the two rightmost images in Fig. 2c were obtained by developing the state with higher mutual friction ($\alpha = 4.7 \times 10^{-2}$). In the simulations, we used a core size of $a_0 \approx 1.7 \times 10^{-5} \text{ mm}$.

Validity and application of the weak turbulence theory

A cascade of KWs can be described within the framework of weak turbulence theory (WTT)^{59,60}, whose validity has been recently confirmed in experiments⁶¹. In principle, WTT can be applied to a variety of systems, both classical^{61–67} and superfluid^{68–72}, given that proper experimental conditions are met. Rotating quantum wave turbulence differs from hydrodynamic quantum turbulence^{73–76} in that the energy cascade is driven by non-linear interactions between waves instead of vortex reconnections.

According to ref. 77, the squared amplitude of KWs can be estimated from

$$A_k^2 = 2 \left(\frac{2\pi^3 c_{\text{LN}}^2}{9} \right)^{1/5} \frac{k_{\text{start}}^{19/15} \epsilon_{\text{KW}}^{1/5}}{k^{3/5} k^{1/3}}, \quad (1)$$

where $c_{\text{LN}} \approx 0.304$ and ϵ_{KW} is the energy cascade rate in the KW cascade. The largest amplitude is at the largest length scale, where $k = k_{\text{start}} = 2.3 \ell^{-1}$. Taking the estimated energy cascade rate $\epsilon_{\text{KW}} = \epsilon_{\text{KW}} \ell^{-2} = 2 \times 10^{-6} \text{ cm}^2 \text{ s}^{-2}$ (Supplementary Discussion 5), we get $A_k \approx 28 \mu\text{m}$ at the largest scale, which is an order of magnitude smaller than the wavelength $\lambda_k \approx 392 \mu\text{m}$. We therefore believe that, to a good approximation, the WTT condition $A_k \ll \lambda_k$ holds and that WTT should

be applicable in our experiment. We use WTT to determine the dependence of τ_{LN} on k_{start} and k_{end} (Supplementary Discussions 5 and 6).

To further confirm the validity of WTT in our experiment, we have tried to limit the fitting of the exponential decay in Fig. 2b to the tail where $\theta < 35^\circ$, corresponding to a ~30% smaller A_k than at the steady state with a tilt angle of $\theta \approx 50^\circ$. Processing only the tail of the relaxation results in an increase in the scatter of the data without qualitative changes. We therefore fit the whole decay for the purposes of extracting the decay time constant τ .

Systematic errors in the mutual friction parameter α

The dissipative mutual friction parameter α used in the analysis has uncertainties from several sources. The parameter α depends on the temperature via the exponential factor $e^{-\Delta/(k_B T)}$ while being linearly proportional to the resonance width of the quartz resonator used as a thermometer^{50,51}. We measure the full resonance curve of the resonator, and extract the temperature from its width. The statistical error in the resonance width is negligible in comparison with systematic errors and can be neglected.

The first source of systematic errors is the conversion from the measured temperature to α . We interpolate in pressure the values of α from ref. 78, where the mutual friction parameter α was measured at several pressures spanning the whole pressure range in this work. We use the theoretically expected pressure dependence for the interpolation, and on the basis of the deviation of the measured points from the theoretical dependence, we estimate that the systematic uncertainty in the conversion of T to α is up to 30%. This uncertainty is the dominant one at higher temperatures ($\alpha \geq 10^{-4}$) and is demonstrated by the horizontal error bar in Fig. 4c for the highest temperature (26.4 bar) data point. The corresponding uncertainty in the vertical direction is smaller than the symbol size in the plot and is not shown.

The second source of systematic error, dominant in the low temperature limit, is the uncertainty in the intrinsic (zero temperature) resonance width of the quartz resonator. At the lowest temperatures ($\alpha < 10^{-5}$, corresponding to $T \approx 0.13T_c$ at 9.6 bar), we estimate that the resulting error in the temperature is smaller than $0.01T_c$. The error bars (both horizontal and vertical) resulting from a change of temperature by $0.01T_c$ are shown in Fig. 4c for the lowest temperature (9.6 bar) data point. This uncertainty decreases quickly with increasing temperature, as the resonance width of the quartz resonator, which depends exponentially on the temperature, exceeds the estimated intrinsic width by an order of magnitude for $\alpha \geq 10^{-4}$.

Data availability

The data that supports the findings of this study are available in Zenodo with the digital object identifier <https://doi.org/10.5281/zenodo.7525698>. Additional data are available from the corresponding author upon reasonable request.

Code availability

The computer code used to support the conclusions of the current study is available from the corresponding author on reasonable request.

References

- Spierings, G. A. C. M. Wet chemical etching of silicate glasses in hydrofluoric acid based solutions. *J. Mater. Sci.* **28**, 6261–6273 (1993).
- Blaauwgeers, R. et al. Quartz tuning fork: thermometer, pressure- and viscometer for helium liquids. *J. Low Temp. Phys.* **146**, 537–562 (2007).
- Riekki, T. S., Rysti, J., Mäkinen, J. T., Sebedash, A. P., Eltsov, V. B. & Tuoriniemi, J. T. Effects of ^4He film on quartz tuning forks in ^3He at ultra-low temperatures. *J. Low Temp. Phys.* **196**, 73–81 (2019).
- Heikkinen, P. J., Autti, S., Eltsov, V. B., Haley, R. P. & Zavjalov, V. V. Microkelvin thermometry with Bose–Einstein condensates of magnons and applications to studies of the AB interface in superfluid ^3He . *J. Low Temp. Phys.* **175**, 681–705 (2014).
- Bradley, D. I. et al. The damping of a quartz tuning fork in superfluid ^3He -B at low temperatures. *J. Low Temp. Phys.* **157**, 476–501 (2009).
- Eltsov, V. B., de Graaf, R., Krusius, M. & Zmeev, D. E. Vortex core contribution to textural energy in ^3He -B below $0.4T_c$. *J. Low Temp. Phys.* **162**, 212–225 (2011).
- Autti, S. et al. Vortex-mediated relaxation of magnon BEC into light Higgs quasiparticles. *Phys. Rev. Res.* **3**, L032002 (2021).
- Hosio, J. J. et al. Propagation of thermal excitations in a cluster of vortices in superfluid ^3He -B. *Phys. Rev. B* **84**, 224501 (2011).
- Schwarz, K. W. Three-dimensional vortex dynamics in superfluid ^4He : line–line and line–boundary interactions. *Phys. Rev. B* **31**, 5782–5804 (1985).
- Hänninen, R. & Baggaley, A. W. Vortex filament method as a tool for computational visualization of quantum turbulence. *Proc. Natl. Acad. Sci. USA* **111**, 4667–4674 (2014).
- Galtier, S. Weak inertial-wave turbulence theory. *Phys. Rev. E* **68**, 015301 (2003).
- Nazarenko, S. *Wave Turbulence* (Springer, 2011).
- Monsalve, E., Brunet, M., Gallet, B. & Cortet, P.-P. Quantitative experimental observation of weak inertial-wave turbulence. *Phys. Rev. Lett.* **125**, 254502 (2020).
- Yarom, E. & Sharon, E. Experimental observation of steady inertial wave turbulence in deep rotating flows. *Nat. Phys.* **10**, 510–514 (2014).
- Yarom, E., Salhov, A. & Sharon, E. Experimental quantification of nonlinear time scales in inertial wave rotating turbulence. *Phys. Rev. Fluids* **2**, 122601 (2017).
- Brunet, M., Gallet, B. & Cortet, P.-P. Shortcut to geostrophy in wave-driven rotating turbulence: the quartet instability. *Phys. Rev. Lett.* **124**, 124501 (2020).
- Brazhnikov, M. Y., Kolmakov, G. V., Levchenko, A. A. & Mezhov-Deglin, L. P. Observation of capillary turbulence on the water surface in a wide range of frequencies. *Europhys. Lett.* **58**, 510–516 (2002).
- Cobelli, P. et al. Different regimes for water wave turbulence. *Phys. Rev. Lett.* **107**, 214503 (2011).
- Lukaschuk, S., Nazarenko, S., McLelland, S. & Denissenko, P. Gravity wave turbulence in wave tanks: space and time statistics. *Phys. Rev. Lett.* **103**, 044501 (2009).
- Efimov, V. B., Kolmakov, G. V., Lebedeva, E. V., Mezhov-Deglin, L. P. & Trusov, A. B. Generation of the second and first sound waves by a pulsed heater in He-II under pressure. *J. Low Temp. Phys.* **119**, 309–322 (2000).
- Rinberg, D., Cherepanov, V. & Steinberg, V. Parametric generation of second sound by first sound in superfluid helium. *Phys. Rev. Lett.* **76**, 2105–2108 (1996).
- Kolmakov, G. Acoustic turbulence in media with two types of sound. *Phys. D* **86**, 470–479 (1995).
- Navon, N., Gaunt, A. L., Smith, R. P. & Hadzibabic, Z. Emergence of a turbulent cascade in a quantum gas. *Nature* **539**, 72–75 (2016).
- Kolmakov, G. V., McClintock, P. V. E. & Nazarenko, S. V. Wave turbulence in quantum fluids. *Proc. Natl. Acad. Sci. USA* **111**, 4727–4734 (2014).
- Walmsley, P. M. & Golov, A. I. Coexistence of quantum and classical flows in quantum turbulence in the $T=0$ limit. *Phys. Rev. Lett.* **118**, 134501 (2017).
- Walmsley, P. M. & Golov, A. I. Quantum and quasiclassical types of superfluid turbulence. *Phys. Rev. Lett.* **100**, 245301 (2008).

75. Cidrim, A., White, A. C., Allen, A. J., Bagnato, V. S. & Barenghi, C. F. Vinen turbulence via the decay of multicharged vortices in trapped atomic Bose–Einstein condensates. *Phys. Rev. A* **96**, 023617 (2017).
76. Barenghi, C. F., Skrbek, L. & Sreenivasan, K. R. Introduction to quantum turbulence. *Proc. Natl. Acad. Sci. USA* **111**, 4647–4652 (2014).
77. Eltsov, V. B. & L'vov, V. S. Amplitude of waves in the Kelvin-wave cascade. *JETP Lett.* **111**, 389 (2020).
78. Mäkinen, J. T. & Eltsov, V. B. Mutual friction in superfluid $^3\text{He-B}$ in the low-temperature regime. *Phys. Rev. B* **97**, 014527 (2018).

Acknowledgements

This work has been supported by the European Research Council (ERC) under the European Union's Horizon 2020 research and innovation programme (grant agreement no. 694248) and by Academy of Finland project no. 332964. Additionally, the research leading to these results has received funding from the European Union's Horizon 2020 research and innovation programme under grant agreement no. 824109 (European Microkelvin Platform). S.A. and V.V.Z. acknowledge funding from UKRI EPSRC (EP/W015730/1) and STFC (ST/T006773/1), and S.A. also acknowledges support from the Jenny and Antti Wihuri Foundation via the Council of Finnish Foundations. V.S.L. was in part supported by NSF-BSF grant no. 2020765. The experiments were performed at the Low Temperature Laboratory, which is a part of the OtaNano research infrastructure of Aalto University and of the European Microkelvin Platform.

Author contributions

The experiments were designed by J.T.M., J.J.H., P.M.W. and V.B.E. The experiments were conducted by J.T.M., S.A., P.J.H., J.J.H., P.M.W. and V.V.Z. The theoretical analysis was carried out by J.T.M., V.S.L., P.M.W. and V.B.E. Numerical calculations were performed by J.T.M., S.A. and R.H. V.B.E. supervised the project. The paper was written by J.T.M., V.S.L., P.M.W. and V.B.E., with contributions from all authors.

Funding

Open access funding provided by Aalto University.

Competing interests

The authors declare no competing interests.

Additional information

Supplementary information The online version contains supplementary material available at <https://doi.org/10.1038/s41567-023-01966-z>.

Correspondence and requests for materials should be addressed to J. T. Mäkinen.

Peer review information *Nature Physics* thanks Ladislav Skrbek and Daniel Lathrop for their contribution to the peer review of this work.

Reprints and permissions information is available at www.nature.com/reprints.